ADVANCED OPTICAL MATERIALS
www.advopticalmat.de

Ultrahigh Raman-Fluorescence Dual-Enhancement in Nanogaps of Silver-Coated Gold Nanopetals

Xinyuan Bi, Zhening Fang, Binge Deng, Lei Zhou, and Jian Ye**

Raman-fluorescence dual-mode enhanced nanoparticles have enormous potential for bioimaging with combined advantages of sensitivity and speed. This is primarily achieved through a trade-off between fluorescence quenching and electromagnetic (EM) enhancement on the plasmonic metal surface, as demonstrated in previous research. A strategy that can minimize EM-field attenuation and temporal photobleaching would be highly desirable. In this study, a novel approach using Raman-fluorescence enhanced dual-mode nanoparticles with the near-infrared fluorescence reporter IR780 directly embedded in the ultra-high EM fields between gold (Au) nanopetals of various morphology and a silver (Ag) coating without a spacer is presented. The results show these nanoparticles to be single-nanoparticle Raman sensitive and that they can generate a fluorescence enhancement factor as high as 1113 experimentally and 2000 by numerical simulation. The random morphology of the nanopetals supports broadband resonances for both fluorescence excitation and emission, resulting in nanowatt detectability, the dual-mode photostability of more than 30 min under continuous laser irradiation, and a long shelf life, making them promising for wide applications in bioimaging with ultra-brightness, low laser power, and long-duration monitoring. In summary, they represent a novel strategy for high-performance Raman-fluorescence enhancement dual-mode nanotags.

1. Introduction

Sensitivity and imaging speed are two critical concerns in bioimaging, especially in clinical applications such as intraoperative guiding,[1–4] residual tumor recognition,[1,5,6] and tissue boundary delineation,[7,8] among others. Currently, surface-enhanced Raman scattering (SERS) nanoparticles (NPs) are gaining popularity in labeled bioimaging due to their superior photostability and higher multiplexing capability compared with fluorescence. This is due to the shorter lifetime, narrower linewidth, and clear spectral fingerprint of the vibrational and rotational modes of their chemical bonds.[9–11]

Through the careful fabrication of plasmonic nanostructures and selection of Raman reporters, SERS can achieve super-high sensitivity down to a single-nanoparticle (SNP) level. However, the commonly used stepwise raster-scan pattern used for large-area SERS imaging is time-consuming.[4,12,13] In comparison, fluorescence images can be collected within seconds on a relatively large scale in a wide-field imaging mode, which is preferred in clinical applications for its time efficiency. Therefore, combining SERS and fluorescence imaging with dual-mode NPs presents a promising solution combining the advantages of both approaches. For example, fluorescence imaging can be used in the first step for an overview picture, and then SERS imaging can be used for specific regions of interest for ultra-sensitive lesion detection.[13,14]

To enable the dual enhancement of fluorescence and Raman scattering, a fluorescence reporter molecule is usually selected and placed adjacent to the plasmonic nanostructures of coinage metals to generate surface-enhanced fluorescence (SEF) and SERS based on the intense electromagnetic (EM) field produced by resonance excitation.[13,15–17] However, fluorescence typically quenches if the reporters are in contact with the metal surface due to near-surface energy transfer (NSET),[18–20] while SERS signals quickly reduce as the metal-reporter distance increases and the EM field weakens based on the fourth power law.[21–23] This trade-off makes it challenging to prepare high-performance dual-mode enhancement NPs.

Consequently, fluorescence enhancements up to three orders of magnitude have been realized in solid assays created by the atomic-layer deposition, by which a thickness-tailorable spacer can be formed at the atomic level to achieve an optimal metal-reporter distance for both modes (≈4 nm, slightly varying in spacers of different refractive indices[24,25]). Approaches using

X. Bi, B. Deng, J. Ye
State Key Laboratory of Oncogenes and Related Genes
School of Biomedical Engineering
Shanghai Jiao Tong University
Shanghai 200030, P. R. China
E-mail: yejian78@sjtu.edu.cn
Z. Fang, L. Zhou
State Key Laboratory of Surface Physics
Key Laboratory of Micro and Nano Photonic Structures (Ministry of Education) and Physics Department
Fudan University
Shanghai 200433, P. R. China
E-mail: phzhou@fudan.edu.cn
J. Ye
Institute of Medical Robotics
Shanghai Jiao Tong University
Shanghai 200240, P. R. China

The ORCID identification number(s) for the author(s) of this article can be found under https://doi.org/10.1002/adom.202300188

DOI: 10.1002/adom.202300188

colloidal NPs have proved much more challenging due to the fabrication challenges of wet chemistry (i.e., coating thickness,[24] random adsorption site of the reporter,[26] etc.).[25] Typical methods for forming the spacer on colloidal NPs include polymer,[24] DNA,[13] SiO_2,[27–29] CTAB,[30,31] and pluronic,[3] among others, most of which only result in single to double-digit fluorescence enhancement factors (EFs) and severe loss of SERS intensity due to the weakened EM field. Crucially, under clinically safe laser intensities (e.g., ultra-low power density),[13] the dual-mode NPs are still not bright enough, and mediocre signals in both channels are unsuitable for long-term monitoring because fluorescence reporters suffer from rapid bleaching under continuous resonance excitation.[32–34] Therefore, it is important to find a new technical route for the design of particles with Raman-fluorescence dual-mode enhancement with adequate sensitivity and photostability using both imaging methods.

Herein, we propose a plasmonic nanostructure to optimize this trade-off between SERS and SEF consisting of a gold (Au) petal core, an embedded-fluorescence reporter, and a silver shell (petals@IR780@Ag) without creating a spacer between core and shell. These NPs exhibited ultra-bright SERS signals and a fluorescence EF as high as 1113. We used finite-element-method (FEM) simulations to investigate the mechanism of the dual-mode enhancement. and found that the nanogaps between the Au nanopetals and the Ag layer create resonances with ultrahigh Q-factors randomly distributed across a broad band of frequencies. This improves the excitation rate and quantum yield simultaneously, promoting dual-mode enhancement and suppressing photobleaching. In addition, we demonstrated nanowatt detectability, improved Raman-fluorescence photostability of more than 30 min under continuous resonant laser excitation, and a long shelf life in both aqueous and dry states. With excellent sensitivity and photostability in both imaging modes, Ag-coated Au nanopetals demonstrate impressive dual-enhancement on the near-metal surface without sacrificing EM intensity, providing a new technical route for dual-mode design and exhibiting great potential for practical, rapid, and sensitive bioimaging.

2. Results and Discussion

2.1. Synthesis and Characterization of Petals@IR780@Ag

The Ag-coated IR780-embedded Au nanopetals, petals@IR780@Ag for short, were fabricated with the layer-by-layer method (**Figure 1**a). In brief, the Au nanopetals were formed by 4-nitrobenzenethiol-induced multi-point nucleation on an Au spherical core, creating numerous external nanogaps among the nanopetals.[12] A near-infrared (NIR) fluorescence reporter, IR780, was directly physio-adsorbed on the Au nanopetals, followed by Ag coating for protection and EM enhancement based on the bimetallic sandwich-like structure. The structures were analyzed under a transmission electron microscope (TEM) combined with element mapping, showing that the numerous nanogaps naturally formed by the rough petal-like structure were still observable after the Ag coating[35,36] (Figure 1b and Figure S1, Supporting Information), though gaps between flat Au and Ag surface cannot be experimentally observed as reported in previous works.[35,37]

The macroscale extinction spectrum was collected with a colloidal aliquot with a UV–vis spectrophotometer, exhibiting two plasmonic resonance peaks at 437 and 556 nm corresponding to the Ag shell and Au petal core, respectively (Figure 1c). The strongest SERS and fluorescence intensities were found under 785 nm laser excitation compared with two alternatives (532 and 638 nm) because it is closest to the maximum absorption of IR780 and can leverage SERS and fluorescence resonance effects (Figure 1d). Furthermore, we observed an obvious enhancement in fluorescence with a fluorescence spectrophotometer and an in vivo optical imaging system (IVIS) (Figure S2, Supporting Information). To quantitatively evaluate the SERS and fluorescence EF achieved by the core-shell structure, we measured the IR780-DMF solution, petals@IR780 (the product before Ag coating), and petals@IR780@Ag using a confocal Raman system.

The spectra obtained show sharp SERS peaks (≈1 nm in linewidth) superimposed on a broad fluorescence background continuum over 50 nm in linewidth[34,38,39] (Figure 1e). It should be noted that the substrate photoluminescence contribution to this background was negligible since the excitation laser wavelength was in the plasmonic off-resonance range.[22,40] This was validated by measurements from NPs of the same structure with a non-fluorescence reporter (Figure S3, Supporting Information).

For quantitative comparison, the spectra were obtained from the probed volume with abundant NPs monodispersed in three independent aliquots, then normalized by the measurement parameters (i.e., acquisition time and laser power) and the number of IR780 fluorescence molecules adsorbed on the NPs (i.e., 2560 molecules per NP, see Note S1, Supporting Information). SERS intensities were computed using the integral area of the IR780-specific band at 1206 cm^{-1} (C-H in-plane deformation[41]).

Petals@IR780@Ag showed single-nanoparticle sensitivity using dual-type single-nanoparticle technique and observation under the correlative Raman imaging and scanning electron microscopy (RISE) under resonance excitation, as reported in our previous works.[36,42] The enhanced EM fields produced by Ag coating create an averaged Raman enhancement 7582 times higher for the same number of fluorescence molecules[43–45] (Figure S6, Supporting Information) compared to petals@IR780. These uncoated nanostructures have already been found to be able to provide a SERS EF beyond 5×10^9.[12]

However, since no Raman signals were observable in IR780 dissolved in DMF in the current system, the SERS EF was not calculated in absolute terms. For SEF, the background spectral maxima were taken as the fluorescence intensities. The petals@IR780@Ag exhibited a fluorescence EF value of 1113 ± 75 compared to bare IR780, higher than the < 2 orders of magnitude enhancement achieved by many previous studies using optimized spacers for SEF on metallic NPs.[9,10] This high fluorescent enhancement could improve sensitivity, accuracy, and safety in clinical applications.

Specifically, the resultant high signal-to-noise/background ratio can enable early detection of some minor lesions labeled with only a few NPs and facilitate the distinction of cancerous from normal tissue to reduce unnecessary damage as much as possible.

Additionally, thanks to enhanced sensitivity, a lower NP injection dose and laser power can be applied to minimize bio-/photo-

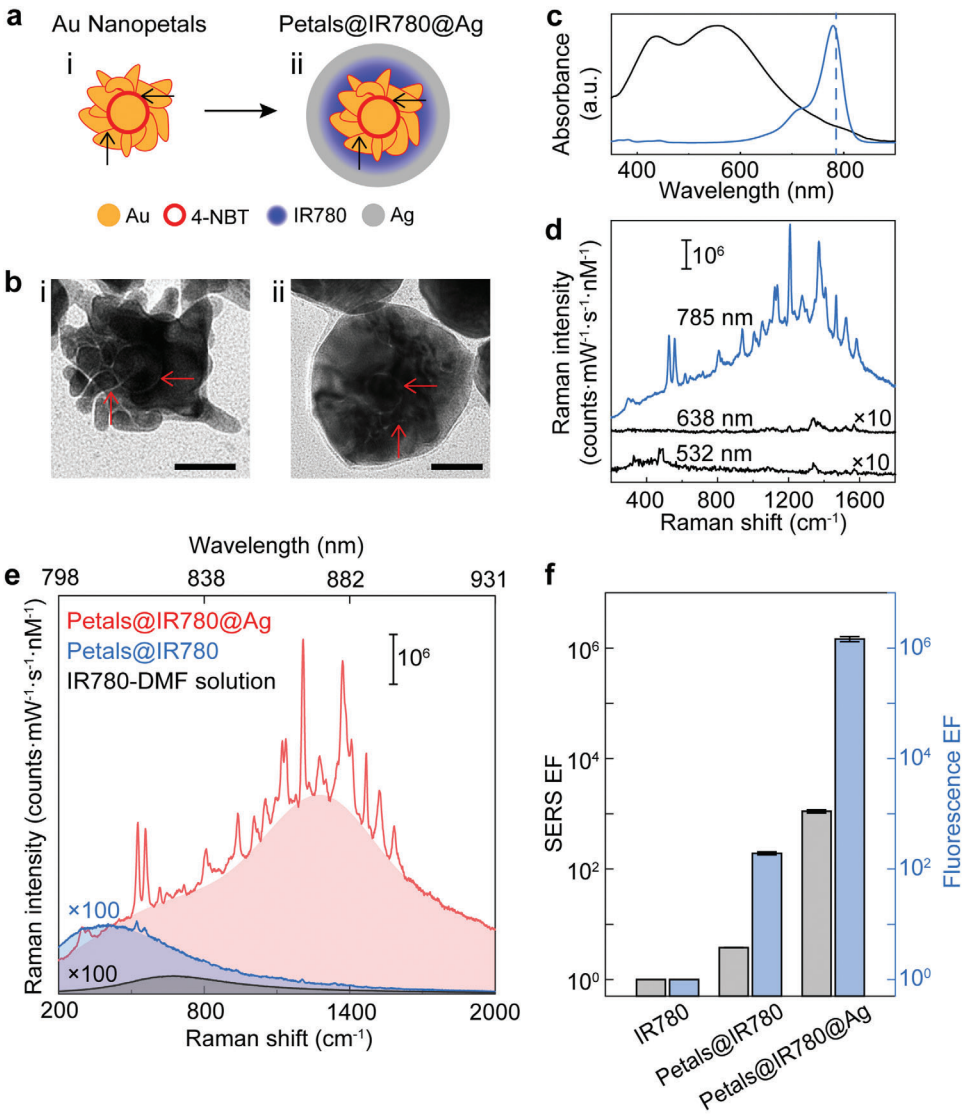

Figure 1. Characterizations of petals@IR780@Ag. a) Schematic illustration and b) TEM images (scale bar: 30 nm) of i) Au nanopetals and ii) petals@IR780@Ag. Horizontal arrows: internal gaps between Au spherical core and Au nanopetals; vertical arrows: external gaps among Au nanopetals. c) Absorbance spectrum of petals@IR780@Ag (black) and the IR780 in methanol solution (blue). The dashed line shows the excitation laser wavelength (785 nm) used in this work. d) SERS spectra of petals@IR780@Ag excited by the laser of 532, 638, and 785 nm. e) Averaged SERS spectra ($n = 3$) of IR780 in DMF solution (black), petals@IR780 (blue), and petals@IR780@Ag (red). The spectra were normalized by the number of adsorbed IR780 per nanoparticle. The fluorescent backgrounds are shown in colored shades under the sharp SERS peaks. f) Histogram of the SERS (black) and fluorescence (blue) EFs with the error bar indicating the standard deviations ($n = 3$).

toxicity. For comparison, petals@IR780 presented only 3.79 ± 0.03 compared to bare IR780, about the same level as seen in previous research[30,31] (Figure 1f). Thus, we deduce that the strong dual-mode signals of petals@IR780@Ag can be attributed to the highly intense EM fields generated by the tips and the external nanogaps tightly confined between the Au nanopetals and Ag coating, in addition to the resonance effect. Detailed computation of SERS and fluorescence EFs is provided in Note S1, Supporting Information. Moreover, an obvious fluorescence redshift has been observed in petals@IR780@Ag towards 870 nm compared with petals@IR780 mainly because of the changed polarity upon the encapsulation of the fluorescence molecules within the NPs, similar to dissolving in DMF (redshift to 830 nm) which is a less polar system comparing to dissolving in methanol[46–48] (Figure S7, Supporting Information). Other mechanisms such as energy transfer to the metal might also account for the reduced energy in fluorescence emission.[49,50] Further validation and mechanisms regarding the enhancement will be discussed later.

2.2. Temporal Photostability and Nanowatt Sensitivity

After confirming the ultra-brightness in both imaging modes, we proceeded to assess the temporal photostability of the NPs, which is another major concern in bioimaging applications such

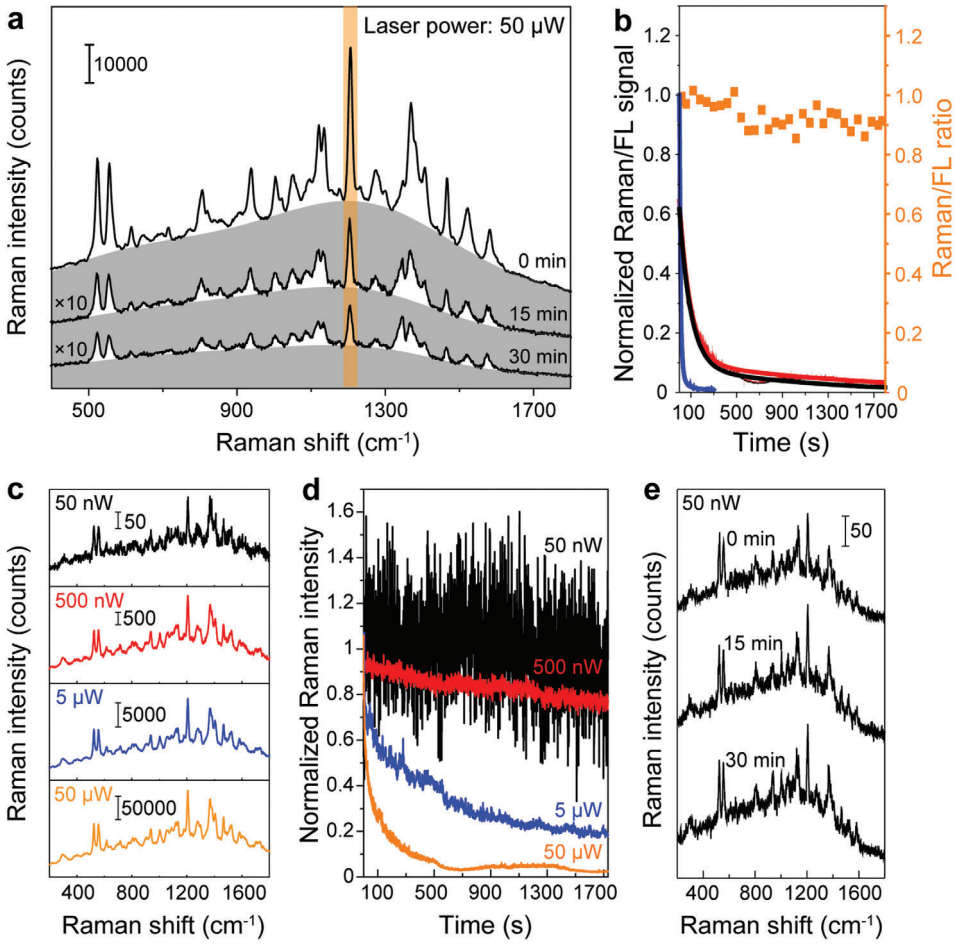

Figure 2. Raman and fluorescence photostability of the petals@IR780@Ag. a) Raman spectra (solid lines) of petals@IR780@Ag and the corresponding fluorescence background (shaded areas) at the three-time points (0, 15, and 30 min) during continuous laser excitation. The characteristic Raman band at 1206 cm^{-1} of IR780 is highlighted in orange. b) Attenuation curves of the Raman signal at 1206 cm^{-1} (black) and fluorescence signal (red). The original attenuation curves are shown by dots and the fitted ones are presented by the thick lines in the corresponding colors. The orange spots represent the ratio of normalized Raman to fluorescence signals with 30 data points displayed for clarity. The fluorescence decay curve of IR780 powder on Si wafer excited by the same parameters (blue) is presented as comparison. c) Raman spectra of petals@IR780@Ag excited by 785 nm-laser of different powers at a fixed site. d) Attenuation curves of different laser powers. e) Raman spectra of petals@IR780@Ag at three-time points (0, 15, and 30 min) by continuous laser excitation (power: 50 nW).

as intraoperative guiding which require long-term monitoring. Although fluorescence molecules are inherently susceptible to photobleaching, it is possible to have a sufficiently intense Raman/fluorescence signal that remains detectable even after prolonged continuous excitation. To evaluate the temporal photostability of petals@IR780@Ag, we prepared dried NP samples on a silica wafer and subjected them to continuous irradiation for 30 min at the same site (785 nm laser, power: 50 μW).

Both SERS and fluorescence signals of IR780, though decreased, remained recognizable with a high signal-to-noise ratio even after 30 min of continuous excitation, indicating their sustainability for long-term distinct visualization (**Figure 2**a). Furthermore, SERS and fluorescence were found to decay at a comparable rate, as indicated by the fluorescence-to-SERS ratio oscillating close to 1 throughout the irradiation (Figure 2b). This synchronous attenuation indicated that the continuous resonance excitation can cause damage to the fluorescence reporter due to EM intensity,[32,34] heating effect,[32,51] photocatalysis,[52,53] etc., leading to a decreased number of active reporters for both types of radiative emission. We looked more closely at the SERS decaying process and found the sudden drops (Figure S8, Supporting Information), demonstrating the bleaching of fluorophores resulting in a fluorescence dark state[54] and ineffective resonant enhancement.

Since the fluorescence-related photobleaching is a stepwise quasi-unimolecular reaction that can be described by the multi-exponential decay model,[55–57] we applied the bi-exponential formula ($y = A_1 e^{-t/\tau_1} + A_2 e^{-t/\tau_2}$) to fit the time-dependent attenuation (Figure 2b, see Figure S9, Supporting Information for the original data).

Herein, the first stage primarily stands for the transient change and the later one for the steady attenuation, consistent with fluorescent multi-step photolysis (see Table S1, Supporting Information for fitting parameters). The obtained time constants (τ) were quite distinct between different stages, but at each stage, SERS and fluorescence exhibited high consistency. Notably,

petals@IR780@Ag exhibited an averaged fluorescence survival time 10 times longer (expressed by the time constants obtained from the bi-exponential fitting[58,59]) than bare IR780 for both the first and the second order time constant (i.e., τ_1 and τ_2) (Figure 2b and Table S1, Supporting Information). Despite the inevitable photobleaching of the fluorophore compared with non-resonance NPs which feature a much milder decay with temporary fluctuations of chemical bonds,[60] petals@IR780@Ag improved the sensitivity significantly, maintaining acceptable recognizability even after long-term resonance excitation.

With the aim of reducing phototoxicity, we explored the sensitivity and photostability by applying lower laser powers (5 μW, 500 nW, and 50 nW) than 50 μW, using a series of neutral density filters (O.D. = 1.0, 2.0, and 3.0). As seen in Figure 2c, SERS and fluorescence signals can be detected with a good signal-to-noise ratio even by nanowatt excitation. In addition, petals@IR780@Ag showed a slower decay rate during the 30-min continuous excitation with decreased laser power. The fitted time constants were positively correlated with the laser power, following the same rule as the power density-dependent photobleaching rate of fluorescence[32,55] (fitting for the 50 nW data points using OriginPro® 2018 failed because the curve was too flat). The remaining signals after the 30-min continuous excitation were 2.9%, 16%, 79%, and 100% of their initial intensity when irradiating at 50 μW, 5 μW, 500 nW, and 50 nW, respectively (Figure 2d and Table S1, Supporting Information). Almost no attenuation was observed under 50 nW irradiation, with SERS intensity at the 30-min time point almost identical to that at the start (Figure 2d,e). Even using a confocal Raman system, the corresponding laser density was only about 640 $W \cdot m^{-2}$, far below the maximum permissible exposure of the skin to laser radiation according to European standards (i.e., 2958 $W \cdot m^{-2}$ corresponding to continuous laser irradiation for 10 to 3×10^4 s at 785 nm).[61] Compared with other research demonstrating nanowatt-level sensitivity with a much higher reporter concentration and longer acquisition time for each spectrum,[62,63] petals@IR780@Ag promise minimal phototoxicity, robust recognition, and real-time tracking with a high acquisition frequency, nanowatt excitation and photostability for longer than 30 min.

2.3. Mechanism of Raman-Fluorescence Dual-Mode Enhancement and Photostability

The petals@IR780@Ag exhibited a large fluorescence enhancement when compared to other studies in the field of SEF with colloidal NPs, while the SERS EF was not as high as in other work[64] despite of the ultra-brightness in the SERS channel which was partially attributed to the resonance enhancement. Therefore, our focus was on understanding the physics that governs fluorescence enhancement during both excitation and emission processes, which may also provide insight into the underlying physics of Raman enhancement. As discussed in ref. [54], the total fluorescence enhancement factor F_E can be written as

$$F_E = F_{exc} \times F_{em} \quad (1)$$

where F_{exc} and F_{em} denote the excitation EFs and quantum yield EF, respectively. In general, high enhancements can be attributed to certain resonance modes at the excitation and/or emission frequencies of the molecule. However, we found that the measured extinction spectrum of our sample only showed two notable peaks at 437 and 556 nm, corresponding to typical resonant frequencies of Ag and Au NPs, respectively (**Figure 3**a). Unfortunately, neither of these two peaks is close to the absorption (780 nm) and emission frequencies (810 nm) of IR780 molecules, indicating that they might not be responsible for the observed enhancement. To resolve this puzzle, we noted that the colloidal NPs may exhibit different morphologies due to the fabrication process, thus supporting resonance modes with a variety of frequencies. The measured far-field extinction spectrum (see Figure 3a) represents an average of these randomly distributed modes and thus does not exhibit any pronounced peaks apart from the two commonly existing plasmonic resonant modes (i.e., 437 and 556 nm). Nevertheless, IR 780 molecules located in the hot spots of these NPs can still be excited by these resonant modes yielding strongly enhanced fluorescence.

We employed FEM simulations to understand the effect of this random distribution of morphologies and resonances, and performed a sample average on multiple configurations to reproduce the observed effects. As shown in Figure 3a, the Au nanocore is covered with multiple petal-like structures, and then coated by an Ag shell. In the fabrication process, nanogaps were likely created between Au nanopetals and Ag shell, which can sustain certain resonance modes with very high quality (Q) factors. To verify our assumption, we studied the far-field extinction spectra of a series of different structures with various geometric parameters and performed a weighted average of the calculated results (see more details in Note S2, Supporting Information). As seen by the red line in Figure 3a, this averaged extinction spectrum has captured all salient features of the measured extinction spectrum. In particular, the calculated spectrum contains two pronounced peaks at similar positions to those discovered experimentally. Interestingly, from detailed analyses of individual spectra of different NPs, we found that the plateau in the calculated spectrum is an average of many resonance peaks with wavelengths randomly distributed in the range of 700–1000 nm. As shown in Figure 3b, the length of nanopetals (see Figure S13, Supporting Information) can significantly alter the extinction spectrum of the NP. As the length of nanopetal varies from 30 to 180 nm, a high-Q peak appears at a wavelength between 700 to 1000 nm (Figure S11, Supporting Information), which has also been seen under a dark-field microscope with single NPs (Figure S15, Supporting Information). The position of such a high-Q peak is dependent on various structural parameters, and multiple high-Q peaks can exist in a single NP, due to the uncontrollable randomness of the fabrication process, leading to a background plateau in the averaged spectrum. Meanwhile, two resonance modes at 437 and 556 nm persisted in the spectra of all different systems (see Figure 3b) and thus were not smeared out by averaging (see Figure 3a).

Having explained the far-field extinction spectra with our model, we then calculated the corresponding F_{exc} and F_{em} factors of NPs with different nanopetal lengths (Figure 3c,d, see Note S3, Supporting Information for details of calculations). As seen in the insets demonstrating the specific field distributions for the resonance of the effective mode, dramatic enhancements exist in the nanogaps and at the tips. Each calculated structure can provide great enhancement in both excitation and emission

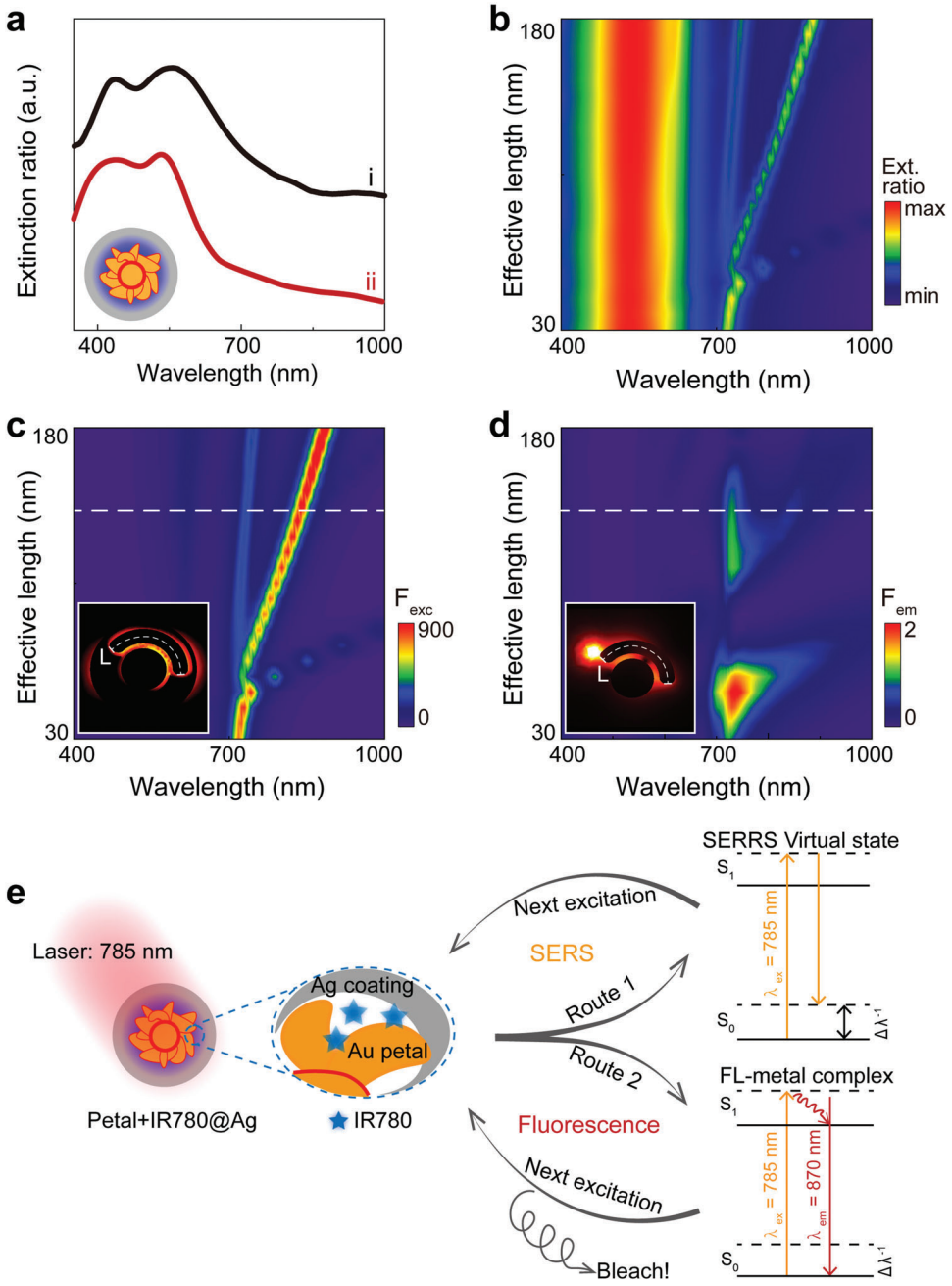

Figure 3. Mechanism of the Raman-fluorescence dual-enhancement and photostability. a) The extinction ratio of the petals@IR780@Ag i) examined (black line) and ii) calculated (red line) together with its schematic illustration. b) The extinction ratio for different lengths of nanopetals, calculated with effective models. c) The spectrum of enhancement of excitation for different lengths of nanopetals, calculated with effective models. d) The spectrum of enhancement of emission for different lengths of nanopetals, calculated with effective models. The insets in panels (c) and (d) show their respective field distributions when the effective length (*L*) is 140 nm as indicated by the dashed lines. e) Schematic illustration of the excitation cycle of the petals@IR780@Ag.

processes for a range of reporter molecules thanks to these random variations in the fabrication process.

On the other hand, photochemical reactions of fluorescence molecules can destroy them, leading to photobleaching if the excited molecules do not emit their energy through radiation. Hence, simply increasing the excitation rate without manipulating the emission process can result in a short lifetime of the molecule, which is undesirable. Fortunately, by increasing the quantum yield of the molecules, our structure could suppress the bleaching rate and enhance the fluorescent ability of the molecules. We calculated the quantum yield of the molecules within the nanogaps (Figure 3d) and found that they were dramatically enhanced compared to IR780, which has an initial quantum yield of 0.078.[65] Furthermore, although our NPs

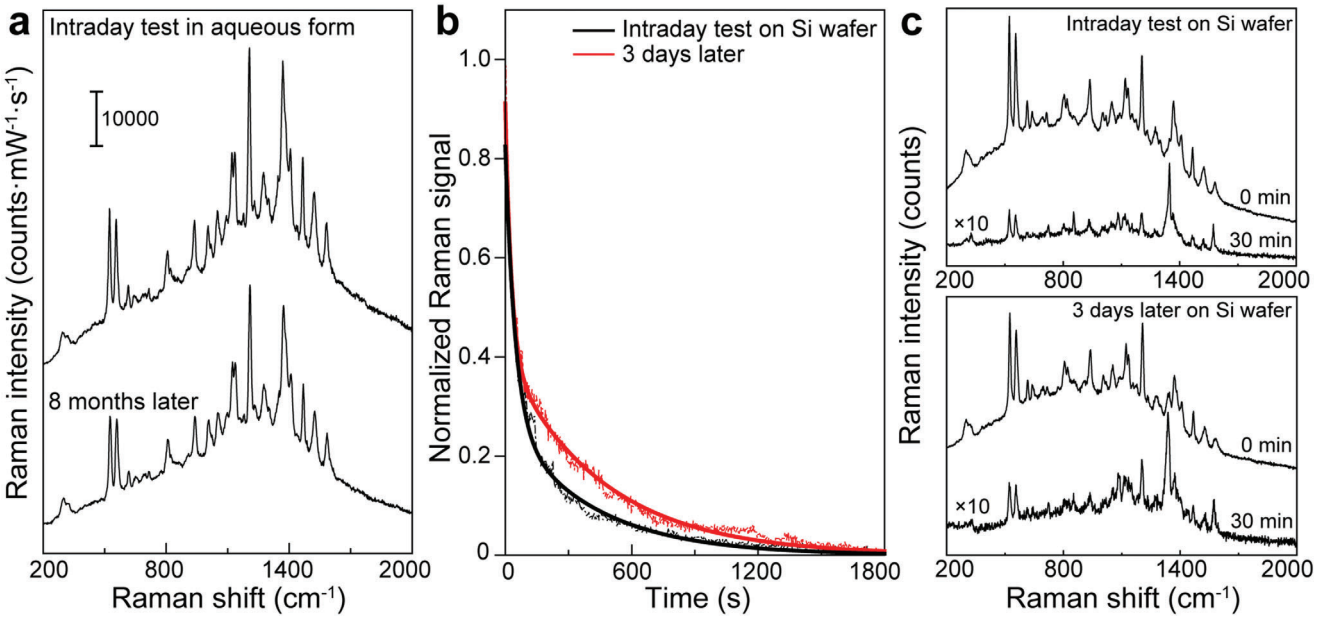

Figure 4. Shelf life. a) SERS spectra of petals@IR780@Ag in aqueous form before and after 8 months of storage. b) Attenuation curves of dried petals@IR780@Ag on silica wafer for 3 days in the ambient conditions and c) their respective time-sampled Raman spectra.

supported resonant modes with very high Q factors, the corresponding quantum yield was not dependent on the working wavelength since the same nanogap mode could enhance both excitation and emission processes since their frequencies were similar. By analyzing the EFs for both excitation and emission processes, we used our model to calculate the overall enhancement of a realistic situation consisting of many different NPs. Our calculations indicate that petals@IR780@Ag can theoretically achieve an enhancement rate of 2000 (see details in Note S3.3, Supporting Information).

For a more intuitive demonstration of the final outcome of the continuous resonance excitation, we present a step-by-step process in Figure 3e. For the petals@IR780@Ag, IR780 molecules were embedded in the nanogaps between Au nanopetals and Ag coating. When the NPs are excited under resonance, there exist two routes of emission: fluorescence or Raman scattering. In each excitation-emission cycle, if the molecule survives undamaged, it goes into the next excitation step for either type of emission; but if it is bleached, it exits. As the number of cycles accumulates, the number of active reporters decreases with the bleaching molecules, resulting in simultaneous bleaching of both SERS and fluorescence signals. Due to the enhancement of both excitation and emission processes of IR780 in the critical nanogaps, petals@IR780@Ag demonstrate ultra-brightness and greatly improved photostability, making them suitable for long-term monitoring with high confidence, that is, suitable for continuous irradiation for longer than 30 min in clinical conditions.

2.4. Off-Site Photostability

In addition to on-site photostability, off-site stability is critical for commercialization. To assess shelf life in aqueous form, we stored the petals@IR780@Ag in CTAC solution for more than 8 months. Neither the SERS nor fluorescence intensities showed any apparent decay (**Figure 4**a), indicating that the expiration period is possibly much longer than this tracked duration. To assess the case where NP-labeled dried specimens may be stored for later examination, petals@IR780@Ag was dropped and dried on a silica wafer, and exposed to ambient conditions for 3 days. When comparing the examination on the day when the samples were freshly made and 3 days after storage, both intensities and attenuation behaviors remained unchanged (Figure 4b,c). This significantly outperforms common fluorescence molecules for clinical use at present such as ICG, which must be used within 4 h after dissolving in water. Therefore, petals@IR780@Ag demonstrated excellent shelf life in both aqueous and dried states, promising easy commercialization and wide application.

3. Conclusion

We have presented a novel plasmonic nanostructure, petals@IR780@Ag, that offers ultra-high SERS-fluorescence dual-mode enhancement at the single-nanoparticle level. By combing resonance excitation with an ultra-intense EM field generated by sandwiching reporter molecules between Au nanopetals and an Ag layer, we achieved an averaged fluorescence EF of 1113 experimentally and 2000 through numerical simulation, as well as an ultra-bright SERS signal. Our FEM simulations revealed that the enhancement was due to the strong near fields in the sandwiched nanogaps and the enhancement of both the excitation rate and quantum yield of the reporter by the randomly grown nanopetals. Thanks to the ultra-high enhancement of both excitation and emission processes, petals@IR780@Ag achieve NIR nanowatt detectability and superior photostability. The particles are promising for many applications in bioimaging in the NIR, where their

superior sensitivity, long-term stability, low phototoxicity, and long shelf life in both aqueous and dried forms all suggest easy commercialization. With these Ag-coated Au nanopetals, we introduce a new strategy for developing SERS-fluorescence dual-mode NPs for efficient clinical bioimaging, including bulk tumor localization and residual tumor detection.

4. Experimental Section

Materials and Instrumentation: Chloroauric chloride ($HAuCl_4 \cdot 4H_2O$), N, N-dimethylformamide (DMF, ≥ 99%), and ethanol (≥ 99.7%) were purchased from Sinopharm Chemical Reagent Co. Ltd. (Shanghai, China). Cetyltrimethylammonium chloride (CTAC, 99%) and sodium borohydride ($NaBH_4$, 98%) were obtained from J&K Chemical Ltd. (Shanghai, China). 4-Nitrobenzenethiol (4-NBT) and IR-780 iodide (IR780, 98%) were acquired from Sigma-Aldrich (Shanghai, China). Silver nitrate ($AgNO_3$, 99.8%) and ascorbic acid (AA, > 99.0%) were bought from Aladdin (China). All materials were used without further purification. Ultrapure water (18.2 MΩ) was used for the experiments. Absorbance spectra were collected by a UV1900 UV–vis spectrophotometer (Aucybest, Shanghai, China). A JEM-2100F transmission electron microscope (JEOL, Tokyo, Japan) was used to obtain the morphologies of the NPs. The fluorescence spectra were measured by an FLS1000 photoluminescence spectrometer (Edinburgh Instruments, England) and the fluorescence image of the NP solution was taken by IVIS Lumina Series III (PerkinElmer, U.S.A.).

Synthesis of Nanoparticles: Petal-like gap-enhanced Raman NPs (Au nanopetals, or called P-GERTs in previous works) and petals@IR780@Ag were synthesized according to the previous works.[12,36,42,66] In brief, 200 µL IR780-DMF (0.16 mM) was mixed and incubated with 1 mL of Au nanopetals (0.25 nM) in 32 °C water bath for 1 h to form Petals@IR780. The resultants were centrifugated and washed with CTAC (50 mM) to remove extra IR780. The supernatant was preserved to evaluate the adsorption rate of IR780 by comparing the peak intensity with the absorbance spectrum of the IR780-DMF solution before adsorption. Ag coating was realized by mixing 400 µL $AgNO_3$ (14.58 mM), 1.875 mL AA (40 mM), 2.5 mL of CTAC (25 mM), and 1 mL of the Petals@IR780 obtained above. The mixtures then experienced ultrasonication and 70 °C incubation in a water bath for 3 h. The petals@IR780@Ag NPs were centrifugated and washed three times and finally redispersed in 25 mM CTAC.

Raman Measurements and Data Processing: Raman measurements were performed on a confocal Raman system (Horiba, XploRA INV) with a laser wavelength of 785 nm if not otherwise indicated. For enhancement evaluations, 5 µL of the aqueous samples were dropped on a silicon wafer and measured through a 10× objective lens. For photostability testing, samples were dripped on a silica wafer after redispersion in water and then dried in the room environment without exposure to light. A 60× objective lens was used for all measurements of the dried samples. In particular, the laser powers lower than 50 µW (i.e., 5 µW, 500 nW, and 50 nW) were achieved by using neutral density filters (Daheng Optics, OD: 1.0, 2.0, and 3.0, respectively) under the configuration of 50 µW. Backgrounds were extracted from all the obtained spectra based on the adaptive iteratively reweighted penalized least squares (airPLS) method (order = 3, $\lambda = 50$). Fluorescence intensities were taken to be the maxima of the extracted background. SERS signals were read by the integral area from 1190–1220 cm^{-1} corresponding to the IR780-characteristic peak at 1206 cm^{-1} from the spectra after background removal. Both signals were also used for the monitoring of temporal photostability. The attenuation curves of SERS and fluorescence intensity were fitted by the bi-exponential function ($y = A_1 e^{-t/\tau_1} + A_2 e^{-t/\tau_2}$) using OriginPro® 2018 software.

Methods for Simulation: All FEM simulations were performed using the commercial software COMSOL Multiphysics. In studying the far-field scattering spectra of the NPs, we considered a spherical space with 800 nm in diameter containing the NP and imposing open boundary conditions. Johnson and Christy's 1972 model was applied to describe the permittivity of Ag and Au. The NP was illuminated by an *x*-polarized Gaussian beam propagating along the *z*-axis with field distribution $E_x = \exp(-x^2/\delta^2 - y^2/\delta^2)$ on its waist-plane in which $\delta = 133$ nm. When studying the fluorescence enhancements of the molecules, the whole process was divided into two parts: excitation and emission. For the excitation part, the same configuration was considered when studying the far-field spectra and illuminated the structure by the same Gaussian beam. The hotspot was identified as the point exhibiting the maximum electric field in the region sandwiched between the Ag shell and the Au nanopetal, and then calculated the local electric fields with and without the NP under the same illuminations, and finally computed the corresponding excitation enhancement. For the emission part, a dipole emitter was put at the same spot as in the emission process, and then computed the total power radiated from the emitter to the free space and the power absorbed by the NP, again in two different cases. With these values numerically obtained in FEM simulations, the authors finally computed the quantum-yield enhancement of the molecule with the NP. More details can be found in Notes S2 and S3, Supporting Information.

Supporting Information

Supporting Information is available from the Wiley Online Library or from the author.

Acknowledgements

The authors thank Benjamin D. Thackray for helping revise the manuscript. The authors acknowledge the financial support from the National Natural Science Foundation of China (No. 82272054 and No. 12221004), the National Key Research and Development Program of China (No. 2022YFA1404700), the Science and Technology Commission of Shanghai Municipality (No. 21511102100), and Shanghai Jiao Tong University (Nos. YG2019QNA28), and the Shanghai Key Laboratory of Gynecologic Oncology.

Conflict of Interest

The authors declare no conflict of interest.

Author Contributions

X.B. and Z.F. contributed equally to this work. J.Y. and X.B. designed this study. X.B. synthesized and characterized the nanoparticles and performed the Raman measurements. Z.F. performed the FEM simulations. All the authors analyzed the data, prepared the manuscript, and have given approval to the final version of the manuscript.

Data Availability Statement

The data that support the findings of this study are available from the corresponding author upon reasonable request.

Keywords

dual-mode nanoparticles, metal-enhanced fluorescence, photosafety, photostability, surface-enhanced Raman scattering

Received: January 24, 2023
Revised: March 7, 2023
Published online: April 7, 2023

[1] Y. Qiu, Y. Zhang, M. Li, G. Chen, C. Fan, K. Cui, J. B. Wan, A. Han, J. Ye, Z. Xiao, *ACS Nano* **2018**, *12*, 7974.

[2] B. Shi, B. Zhang, Y. Zhang, Y. Gu, C. Zheng, J. Yan, W. Chen, F. Yan, J. Ye, H. Zhang, *Acta Biomater.* **2020**, *104*, 210.
[3] T. Nagy-Simon, M. Potara, A. M. Craciun, E. Licarete, S. Astilean, *J. Colloid Interface Sci.* **2018**, *517*, 239.
[4] Y. Zhang, J. Qian, D. Wang, Y. Wang, S. He, *Angew. Chem., Int. Ed.* **2013**, *52*, 1148.
[5] M. C. Boonstra, B. Tolner, B. E. Schaafsma, L. S. F. Boogerd, H. A. J. M. Prevoo, G. Bhavsar, P. J. K. Kuppen, C. F. M. Sier, B. A. Bonsing, J. V. Frangioni, C. J. H. van de Velde, K. A. Chester, A. L. Vahrmeijer, *Int. J. Cancer* **2015**, *137*, 1910.
[6] S. van Keulen, N. Nishio, S. Fakurnejad, A. Birkeland, B. A. Martin, G. Lu, Q. Zhou, S. U. Chirita, T. Forouzanfar, A. D. Colevas, N. S. van den Berg, E. L. Rosenthal, *J Nucl Med* **2019**, *60*, 758.
[7] Z. Bao, Y. Zhang, Z. Tan, X. Yin, W. Di, J. Ye, *Biomaterials* **2018**, *163*, 105.
[8] J. Song, N. Zhang, L. Zhang, H. Yi, Y. Liu, Y. Li, X. Li, M. Wu, L. Hao, Z. Yang, Z. Wang, *Int. J. Nanomed.* **2019**, *14*, 2757.
[9] C. Joyce, S. M. Fothergill, F. Xie, *Mater. Today Adv.* **2020**, *7*, 100073.
[10] M. A. Badshah, N. Y. Koh, A. W. Zia, N. Abbas, Z. Zahra, M. W. Saleem, *Nanomaterials* **2020**, *10*, 1749.
[11] Me. Wang, Mi. Wang, G. Zheng, Z. Dai, Y. Ma, *Nanoscale Adv.* **2021**, *3*, 2448.
[12] Y. Zhang, Y. Gu, J. He, B. D. Thackray, J. Ye, *Nat. Commun.* **2019**, *10*, 3905.
[13] S. Pal, A. Ray, C. Andreou, Y. Zhou, T. Rakshit, M. Wlodarczyk, M. Maeda, R. Toledo-Crow, N. Berisha, J. Yang, H. T. Hsu, A. Oseledchyk, J. Mondal, S. Zou, M. F. Kircher, *Nat. Commun.* **2019**, *10*, 1926.
[14] M. Wang, M. Wang, G. Zheng, Z. Dai, Y. Ma, *Nanoscale Adv.* **2021**, *3*, 2448.
[15] A. R. Guerrero, Y. Zhang, R. F. Aroca, *Small* **2012**, *8*, 2964.
[16] P. C. White, *Sci. Justice* **2000**, *40*, 113.
[17] H. Xu, X.-H. Wang, M. P. Persson, H. Q. Xu, M. Käll, P. Johansson, *Phys. Rev. Lett.* **2004**, *93*, 243002.
[18] C. M. Walters, C. Pao, B. P. Gagnon, C. R. Zamecnik, G. C. Walker, *Adv. Mater.* **2018**, *30*, 1705381.
[19] Y. Wei, L. Li, D. Sun, Y. Zhu, G. Tian, *Opt. Commun.* **2018**, *427*, 426.
[20] Y. Zhang, W. Chen, T. Fu, J. Sun, D. Zhang, Y. Li, S. Zhang, H. Xu, *Nano Lett.* **2019**, *19*, 6284.
[21] L. A. Lane, X. Qian, S. Nie, *Chem. Rev.* **2015**, *115*, 10489.
[22] A. I. Pérez-Jiménez, D. Lyu, Z. Lu, G. Liu, B. Ren, *Chem. Sci.* **2020**, *11*, 4563.
[23] J. F. Li, Y. F. Huang, Y. Ding, Z. L. Yang, S. B. Li, X. S. Zhou, F. R. Fan, W. Zhang, Z. Y. Zhou, D. Y. Wu, B. Ren, Z. L. Wang, Z. Q. Tian, *Nature* **2010**, *464*, 392.
[24] R. Kato, M. Uesugi, Y. Komatsu, F. Okamoto, T. Tanaka, F. Kitawaki, T.-A. Yano, *ACS Omega* **2022**, *7*, 4286.
[25] B. Song, Z. Jiang, Z. Liu, Y. Wang, F. Liu, S. B. Cronin, H. Yang, D. Meng, B. Chen, P. Hu, A. M. Schwartzberg, S. Cabrini, S. Haas, W. Wu, *ACS Nano* **2020**, *14*, 14769.
[26] K. Zhang, Y. Wang, M. Wu, Y. Liu, D. Shi, B. Liu, *Chem. Sci.* **2018**, *9*, 8089.
[27] Y.-T. Liu, X.-F. Luo, Y.-Y. Lee, I. C. Chen, *Dyes Pigm.* **2021**, *190*, 109263.
[28] A. R. Guerrero, R. F. Aroca, *Angew. Chem., Int. Ed.* **2011**, *50*, 665.
[29] X. Bian, G. Zhang, B. Liu, J. Yang, *J. Nanopart. Res.* **2022**, *24*, 20.
[30] A. M. Gabudean, M. Focsan, S. Astilean, *J. Phys. Chem. C* **2012**, *116*, 12240.
[31] H. I. Khan, G. A. Khan, S. Mehmood, A. D. Khan, W. Ahmed, *Spectrochim. Acta, Part A* **2019**, *220*, 117111.
[32] C. M. Galloway, C. Artur, J. Grand, E. C. Le Ru, *J. Phys. Chem. C* **2014**, *118*, 28820.
[33] A. Merlen, F. Lagugné-Labarthet, E. Harté, *J. Phys. Chem. C* **2010**, *114*, 12878.
[34] C. M. Galloway, P. G. Etchegoin, E. C. Le Ru, *Phys. Rev. Lett.* **2009**, *103*, 063003.
[35] N. G. Khlebtsov, L. Lin, B. N. Khlebtsov, J. Ye, *Theranostics* **2020**, *10*, 2067.
[36] Y. Gu, X. Bi, J. Ye, *J. Mater. Chem. B* **2020**, *8*, 6944.
[37] Y. Feng, Y. Wang, H. Wang, T. Chen, Y. Y. Tay, L. Yao, Q. Yan, S. Li, H. Chen, *Small* **2012**, *8*, 246.
[38] Y. Wang, B. Yan, L. Chen, *Chem. Rev.* **2013**, *113*, 1391.
[39] J. R. Lakowicz, *Principles of Fluorescence Spectroscopy*, Springer, Boston, MA **2006**.
[40] S. Zhu, B. Deng, F. Liu, J. Li, L. Lin, J. Ye, *ACS Appl. Mater. Interfaces* **2022**, *14*, 8876.
[41] G. Perna, M. Lasalvia, C. Gallo, G. Quartucci, V. Capozzi, *Open Surf. Sci. J.* **2013**, *5*, 1.
[42] X. Bi, Y. Gu, J. Ye, *ACS Appl. Nano Mater.* **2020**, *3*, 6987.
[43] S. Pande, S. K. Ghosh, S. Praharaj, S. Panigrahi, S. Basu, S. Jana, A. Pal, T. Tsukuda, T. Pal, *J. Phys. Chem. C* **2007**, *111*, 10806.
[44] Y. Zhou, C. Lee, J. Zhang, P. Zhang, *J. Mater. Chem. C* **2013**, *1*, 3695.
[45] E. Wiercigroch, P. Swit, A. Brzozka, Ł. Pięta, K. Malek, *Microchim. Acta* **2021**, *189*, 32.
[46] C. Reichardt, *Chem. Rev.* **1994**, *94*, 2319.
[47] Y. C. Tsai, P. Vijayaraghavan, W. H. Chiang, H. H. Chen, T. I. Liu, M. Y. Shen, A. Omoto, M. Kamimura, K. Soga, H. C. Chiu, *Theranostics* **2018**, *8*, 1435.
[48] Y. Kuang, K. Zhang, Y. Cao, X. Chen, K. Wang, M. Liu, R. Pei, *ACS Appl. Mater. Interfaces* **2017**, *9*, 12217.
[49] H. Chen, T. Ming, L. Zhao, F. Wang, L.-D. Sun, J. Wang, C.-H. Yan, *Nano Today* **2010**, *5*, 494.
[50] Y.-T. Liu, X.-F. Luo, Y.-Y. Lee, I. C. Chen, *Dyes Pigm.* **2021**, *190*, 109263.
[51] R. C. Maher, C. M. Galloway, E. C. Le Ru, L. F. Cohen, P. G. Etchegoin, *Chem. Soc. Rev.* **2008**, *37*, 965.
[52] P. B. Santos, J. J. Santos, C. C. Corrêa, P. Corio, G. F. S. Andrade, *J. Photochem. Photobiol., A* **2019**, *371*, 159.
[53] J.-H. Oh, H. Lee, D. Kim, T.-Y. Seong, *Surf. Coat. Technol.* **2011**, *206*, 185.
[54] W. Zhao, X. Tian, Z. Fang, S. Xiao, M. Qiu, Q. He, W. Feng, F. Li, Y. Zhang, L. Zhou, Y. W. Tan, *Light: Sci. Appl.* **2021**, *10*, 79.
[55] C. Eggeling, J. Widengren, R. Rigler, C. A. M. Seidel, *Anal. Chem.* **1998**, *70*, 2651.
[56] J. Enderlein, R. Erdmann, *Opt. Commun.* **1997**, *134*, 371.
[57] P. F. Williams, D. L. Rousseau, S. H. Dworetsky, *Phys. Rev. Lett.* **1974**, *32*, 196.
[58] T. Hirschfeld, *Appl. Opt.* **1976**, *15*, 3135.
[59] S. Wennmalm, R. Rigler, *J. Phys. Chem. B* **1999**, *103*, 2516.
[60] Y. Gu, Y. Zhang, Y. Li, X. Jin, C. Huang, S. A. Maier, J. Ye, *RSC Adv.* **2018**, *8*, 14434.
[61] No. EN 60825-1:2014 Safety of Laser Products-Part 1: Equipment Classification and Requirements, European Committee for Electrotechnical Standardization.
[62] S. Chen, X. Li, Y. Guo, J. Qi, *Analyst* **2015**, *140*, 3239.
[63] J. Long, H. Yi, H. Li, Z. Lei, T. Yang, *Sci. Rep.* **2016**, *6*, 33218.
[64] J.-E. Shim, Y. J. Kim, J.-H. Choe, T. G. Lee, E.-A. You, *ACS Appl. Mater. Interfaces* **2022**, *14*, 38459.
[65] G. Chapman, M. Henary, G. Patonay, *Anal. Chem. Insights* **2011**, *6*, 29.
[66] Y. Zhang, Y. Qiu, L. Lin, H. Gu, Z. Xiao, J. Ye, *ACS Appl. Mater. Interfaces* **2017**, *9*, 3995.